Article

Not peer-reviewed version

Influence of Te Incorporated LaCoO3 on Structural, Morphology and Magnetic Properties

Jhelai Sahadevan , S Esakki Muthu * , P Sivaprakash , Ikhyun Kim * , N Padmanathan , E Eswaramoorthi

Posted Date: 29 May 2023

doi: 10.20944/preprints202305.1993.v1

Keywords: Rhombohedral; Hdtrothermal synthesis; chemical reduction; Oxygen deficiency; Low spin state; Ferromagnetism

Article

Influence of Te incorporated $LaCoO_3$ on Structural, Morphology and Magnetic Properties

Jhelai Sahadevan [1,$], S. Esakki Muthu [1,*], P. Sivaprakash [2,$], Ikhyun Kim [2,*], N. Padmanathan [1,3] and V. Eswaramoorthi [4]

[1] Department of Physics, FASCM, Karpagam Academy of Higher Education, Coimbatore and India
[2] Department of Mechanical Engineering, Keimyung University, Daegu, 42601, South Korea
[3] Micro-Nano System Centre, Tyndall National Institute, University College Cork, Cork Ireland
[4] Department of Physics, Karpagam College of Engineering, Coimbatore, India
[$] Authors equally contributed to this work
* Correspondence: Authors: sanrajson@yahoo.com (SEM) & kimih@kmu.ac.kr (IK)

Abstract: A high perovskite activity is sought for use in magnetic applications. In this paper, we present the simple synthesis of (2.5 and 5%) Tellurium-impregnated-$LaCoO_3$ (Te-LCO), Te and $LaCoO_3$ (LCO) by using a ball mill, chemical reduction, and hydrothermal synthesis, respectively. We also explored the structure stability along with the magnetic properties of Te-LCO. Te has a rhombohedral crystal structure, whereas Te-LCO has a hexagonal crystal system. The reconstructed Te was imbued with LCO that was produced by hydrothermal synthesis; as the concentration of the imbuing agent grew, the material became magnetically preferred. According to the X-ray photoelectron spectra, the oxidation state of the cobaltite is one that is magnetically advantageous. As a result of the fact that the creation of oxygen-deficient perovskites has been shown to influence the mixed ($Te^{4+/2-}$) valence state of the incorporated samples, it is abundantly obvious that this process is of utmost significance. The TEM image confirms the inclusion of Te in LCO. The samples start out in a paramagnetic state (LCO), but when Te is added to the mixture, the magnetic state shifts to a weak ferromagnetic one. It is at this point that hysteresis occurs due to the presence of Te. Despite being doped with Mn in our prior study, rhombohedral LCO retains its paramagnetic characteristic at room temperature (RT). As a result, the purpose of this study was to determine the impacts of RT field dependency of magnetization (M-H) for Te-impregnated LCO in order to improve the magnetic properties of RT because it is a low-cost material for advanced multi-functional and energy applications.

Keywords: rhombohedral; hydrothermal synthesis; chemical reduction; oxygen deficiency; low spin state; ferromagnetism

1. Introduction

Perovskites are one of the most fascinating types of solid materials, exhibiting a wide range of physical events and characteristics. Extensive research has been conducted on ABO_3-type perovskites with the general formula $Ln_{1-x}A_xMO_3$ or $LnB_xM_{1-x}O_3$(Ln-Lanthanides and M-dopant). Researchers have been intrigued by nano crystallite magnetic cobaltite due to its outstanding magnetic and electric capabilities for decades.Single-phase $LaCoO_3$ perovskite is a good example of ceramic materials and is utilised in essential applications like ZrB_2+10 wt.%SiC for leading edges and nose cones in hypersonic vehicles and $LaCoO_3$ for solid oxide fuel cell cathodes [1]. A wide variety of practical applications are made possible by many intrinsic perovskite materials features due to the continuous interaction between structure and properties. Ferroelectricity [2–4], semi-conductivity [5,6], superconductivity [5,6], piezoelectricity [7,8], thermoelectricity [9], colossal magnetoresistance, ferromagnetism [10], half-metallic transport [11,12] are just some of the fascinating physical and chemical properties of perovskites. These oxides are increasingly being used in electronic and magnetic materials, automotive exhaust, water splitting catalysts, fuel cells, battery electrode materials [13], gas sensors, humidity sensors, microwave devices, high-density data storage, magnetic ferrofluids, magnetic switches, MRI, high-frequency, and power devices are among the applications for these materials [2]. As demonstrated by the discovery of superconductivity in $Na_{0.3}CoO_2.1.3H_2O$, the fact that cobalt cations can assume multiple oxidation and spin states is the root cause of the wide range of observable physical features of cobaltites [14]. Specifically, the LCO perovskite is a classic example of thermally aided spin state transitions of trivalent cobalt [15,16]. Integration of divalent/trivalent or magnetic/nonmagnetic dopant ions into a lattice result in a drastic alteration of the structure and other properties defined by cation distribution. Dopant choice is needed to get the desired improvement in the unaltered perovskite cobaltite. In particular, the shift from paramagnetic (PM) to ferromagnetic (FM) at the Curie temperature (T_C) and the accompanying insulator–metal transition (TIM) in the case of manganite and cobaltite have been known for some time. These include high conductivity, magnetic properties, excellent performance as a cathode or an anode, a high Seebeck coefficient, and various forms of oxygen vacancy order. The $LaCoO_3$ perovskite, in instance, is a famous example of thermally aided trivalent cobalt spin state transitions. It has a nonmagnetic insulator ground state with only low-spin (LS) Co^{3+}, but its magnetic susceptibility rises with temperature up to 100 K due to a transition from the LS to the intermediate-spin (IS) state. A second spin-state transition is then inferred from a shift in transport characteristics above 500 K from an activated regime (0.1 eV at 100 K) to a metallic regime (~1 mΩ cm), which corresponds to a conversion to high-spin (HS). The energetic proximity of the various Co^{3+} spin-states (LS, IS, and HS), as demonstrated by these two spin-state transitions, is also highlighted by the dramatic effect of a small amount of doping on physical attributes [17].

Ferroelastic materials having rhombohedral lattices are particularly fascinating. Stretching along one of the perovskite unit cell's four body diagonals distorts the parent cubic structure, causing ferro elasticity [18]. As previously reported, LCO is ferromagnetic at low temperatures [19], and B site incorporation increases the magnetic properties. The complicated interplay between the interatomic exchange interaction energy (Δ_{ex}) and the crystal field splitting energy (Δ_{cf}) controls the active spin crossover of Co ion's low and high spin states. A modest structural disruption brought on by strain can have a considerable effect since Δ_{cf} is particularly sensitive to changes in O-Co bond length and Co-O-Co bond angle [20,21].

Microwave heating, chemical co-precipitation, sol-gel auto-combustion [22], micro- and nano-emulsions, hydrothermal techniques, high-temperature breakdown, and reverse micelle have all been used to create cobaltite magnetic nanoparticles (NPs) [23–25]. The best way to produce $LaCoO_3$ is through hydrothermal synthesis because it is easy, cheap, and safe for the environment. One of the most important aspects of our study was the hydrothermal method, which allowed us to produce superior perovskite precipitates with the required stoichiometry and microstructure. Hydrothermal synthesis of LCO by L. Tepech-Carrillo.et.al., followed by a study of LCO structure at different calcination temperatures is elaborated. However, they did not look into LCO or Te-LCO composites' structures or magnetic properties. Since Te(2.5% and 5%) in $LaCoO_3$ modifies the magnetic properties, we are attracted in studying the magnetic properties and structural analysis of this material [26].Unlike our prior work, in which we discovered no change in paramagnetic states at RT when doping Mn into LCO, we found that the Te inclusion in LCO has impacted the RT magnetic characteristics of LCO crystals. Therefore, we set out to improve LCO's magnetic characteristics when it was exposed to RT. After discovering LT ferromagnetism in Mn-doped LCO, we set out to investigate whether or not the same phenomenon would occur in Te-incorporated LCO.

2. Materials and Methods

2.1. Materials

2.1.1. Materials for the preparation of Te (Method 1).

The precursor materials used for the preparation of Te are Tellurium dioxide (TeO_2) [Sigma Aldrich], and Sodium borohydride ($NaBH_4$) [Merck].

2.1.2. Materials for the preparation of $LaCoO_3$ (Method 2).

The precursor materials used for the preparation of LCO are Lanthanum (III) nitrate hexahydrate ($La(NO_3)_3{\cdot}6H_2O$) [Merck], Cobalt (II) Nitrate Hexahydrate ($Co(NO_3)_2{\cdot}6H_2O$) [Merck], Ammonia Solution About 25% (NH_4OH) [Merck], and Sodium Hydroxide (NaOH) [Merck].

2.1.3. Materials for the preparation of Te (2.5%) impregnated $LaCoO_3$ and Te (5%) impregnated $LaCoO_3$(Method 3).

The materials obtained after preparation of method 1 and method 2 are Te and $LaCoO_3$. These two materials are used to prepare Te impregnated $LaCoO_3$.All of the chemicals are reagent grade with high purity (99.9%) and can be used straight out of the package.

2.2. Methods

2.2.1. Method 1: The preparation of Te.

From room temperature (RT) to boiling point (BP), 100 ml of $C_2H_6O_2$ and TeO_2 (2 g wt.) were homogenously mixed using a magnetic stirrer in a silicon oil bath to maintain a temperature of 180 ºC in a double-neck round-bottomed flask equipped with a reflux cooler for 2 hours or longer. The ratio of salt to reductant was maintained at 1:4. After 2 h, 8 g of $NaBH_4$ was added slowly into the mixture with the evolution of gases. While introducing $NaBH_4$, regular personnel protective equipment (PPE) precautions and other safety measures were taken. After adding the reducing agent, the reaction mixtures were stirred for two hours and cooled to RT naturally. The ultimate precipitate was centrifuged and repeatedly washed with DI-water, acetone, and ethanol before being dried at RT Equation depicts the reaction of the sodium borohydride and tellurium dioxide (1).

$$TeO_2 + C_2H_6O_2 \xrightarrow{180\ ^{\circ}\mathrm{C}||NaBH_4} TeO(OH) + \frac{1}{2}H_2^{\uparrow} + \frac{1}{2}B_2H_4 + NaOH \qquad (1)$$

TeO (OH^-) is formed in two steps (Eq. 1), involving reduction by hydrogenation. Initially, TeO_2 was reduced to equivalent ions and hydrogenated oxygen (H^+O) was collected at the surface. The evolved H_2 may dissociate into H atoms or ions during the reduction process.

2.2.2. Method 2: The preparation of $LaCoO_3$.

We have briefly discussed the hydrothermal synthesis of LCO in our previous report [18].

2.2.3. Method 3: The preparation of Te impregnated $LaCoO_3$.

The third method is ball milling of the samples obtained from the first two methods. The ball-milling of Te and LCO is as follows: 2.5 and 5% Te are mixed with 97.5 and 95% LCO by weight respectively and well ground for 10 hours with intervals of 30 minutes to avoid settling of powder on the sides of the ball-mill container. After the ball milling, the material is taken for further studies.

2.3. Characterisation Technique

To investigate the phase transformations at ambient temperatures, a CuK-alpha radiation was utilised in an Empyrean Malvern Panalytical X-ray Powder Diffractometer. A field emission scanning electron microscope (FESEM) equipped with energy dispersive X-Ray spectroscopy (EDAX) was used to investigate the surface topography and composition of the microstructure. The vibrational modes of the materials are studied using a confocal micro-Raman microscope (WiTec Alpha 300, Germany) equipped with AFM imaging and a He-Ne laser as the excitation source (λ-exc = 532 nm) in a backscattering setup. In order to investigate the chemical composition of the surface, we used X-ray photo-electron spectroscopy (XPS) with Al K-alpha X-rays (Thermo Scientific, UK) was utilised. A JEOL JEM 2100 HRTEM was utilised for microscopic examination and evaluation. The effect of a magnetic field strength of 5 T on the material's magnetization (M-H) at room temperature was investigated using SQUID-MPMS (Quantum Design, USA).

doi:10.20944/preprints202305.1993.v1

3. Results and Discussion

3.1. *Powder X-Ray Diffraction (P-XRD) of Te Incorporated LaCoO3*

For parent LCO and two different concentrations of 2.5% and 5%Te-LCO, the powder XRD patterns were taken. The standard single-phase crystallite perovskite structure of LCO (JCPDS 48-0123) can be used to assign all of the diffraction peaks of the prepared samples, proving that the perovskite structures are well preserved after Te in-corporation as shown in Figure 1. There were no peaks that could be attributed to impurities. Furthermore, an enlarged scale of the higher intensity diffraction peaks of the prepared samples (2θ range: 30-38°) is shown at the outset of Figure 1 and reveals a slight shift towards higher 2θ as the concentration of Te^{2-} (ionic radius 207 pm) increases, which has been attributed to Te's larger ionic radius compared with that of Te. The crystal planes of rhombohedral LCO are marked in Figure 1 with reference to standard JCPDS Card No. 48-0123. To understand the reduction in TeO_2, we took XRD for both parent and reduced Te, which is shown in Figure 2. TeO_2 is successfully reduced to Te, as shown by the XRD data, which is supported by the ICSD collection codes 34-422 and 65-3048 for TeO_2 and Te, respectively. The crystal structure transforms from tetragonal to hexagonal during the reduction of TeO_2 to Te, as reported in the reference data sheet. Table 1 illustrates the lattice parameter, crystal system, space group, and crystallite size of TeO_2, Te, LCO, 2.5% Te-LCO, and 5% Te-LCO. The average crystal size was determined using the Debye-Scherrer formula, and the lattice parameters were determined using unit cell software.

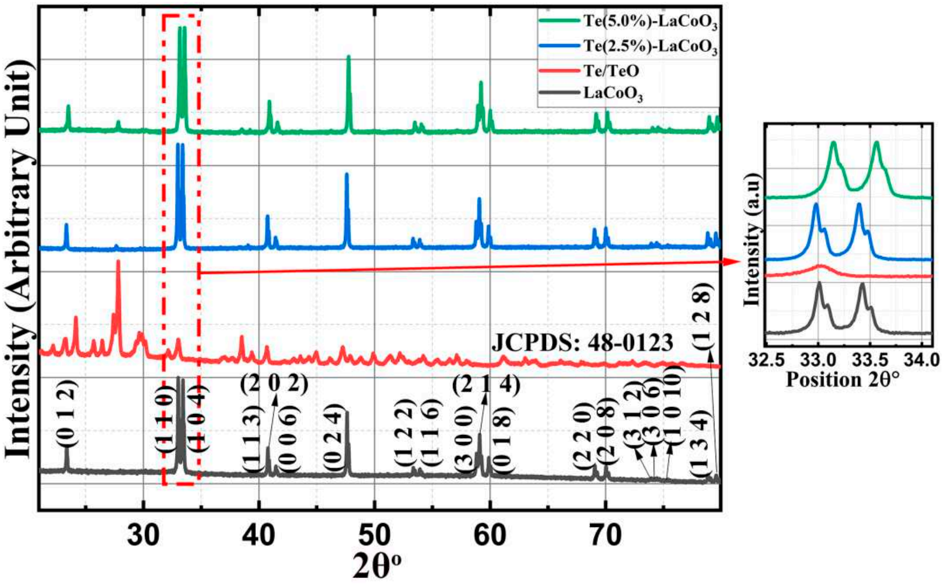

Figure 1. X-ray Diffraction of LCO, Te, & Te(2.5 & 5%)-LCO. Outset shows the magnified image of high intensity peaks of LCO, Te, & Te(2.5 & 5%)-LCO.

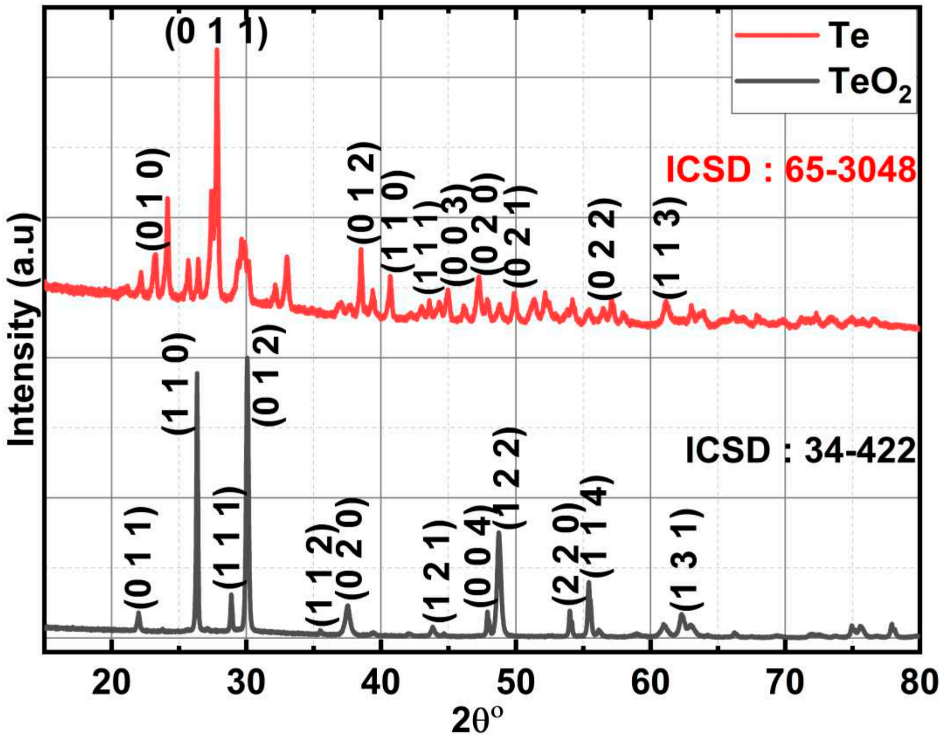

Figure 2. X-ray Diffraction of TeO_2 and Te.

Table 1. The crystallite size and lattice parameter of TeO_2, Te, LCO, LCO/Te(2.5%) and LCO/Te(5%).

Composition	**Crystal System**	**Space Group**	**Crystallite size (nm)** $D = \frac{0.9\lambda}{\beta cos\theta}$	**Lattice Parameter (Å)**		
				a	b	c
TeO_2	Tetragonal	$P4_12_12$	26.80514	5.40681	5.40865	13.20149
Te	Hexagonal	$P3_121$	28.33724	4.19097	4.19123	5.98099
$LaCoO_3$	Rhombohedral	$R\bar{3}c$	43.42469	5.41768	5.39366	13.13084
2.5% Te/LCO	Rhombohedral	$R\bar{3}c$	31.59925	5.42428	5.39256	13.1579
5% Te/LCO	Rhombohedral	$R\bar{3}c$	31.59925	5.42681	5.39434	13.20149

3.2. Raman Spectrum analysis of Te Incorporated $LaCoO_3$

Hydrothermally produced LCO, chemically reduced Te, and Te-impregnated LCO are analysed for their chemical distribution using Raman spectroscopy. In Figure 3, Raman scattering measurements of LCO, Te, 2.5% Te-LCO, and 5% Te-LCO are displayed. The primeval LCO has weak Raman signals compared to Te, 2.5 percentage Te–LCO, and 5 percentage Te-LCO, whereas the 2.5 and 5 percentage Te in cooperated LCO have good Te signals, which match the Te and have a slight shift and have a significant Raman characteristic peak. The Co-O-Co stretching mode in strongly deformed CoO_6 may be related to the newly widened band at 516 cm^{-1} [27]. The E_g symmetry, which may be related to exterior mode (La-O) vibration, is responsible for the 116 and 140 cm^{-1} peaks [28,29]. Te exhibits strong Raman-active phonon modes as a result of its high atomic number and electronic polarizability. Three atoms make up each tellurium unit cell, which is arranged in an unending chain parallel to the c-axis. One A_1 mode and two degenerate E modes, which are identified by rigid-chain rotation across the a- and b-axes and which fit into the Te lattice's D_3 symmetry group, are indicated by the Raman spectra. The week bands at 103 cm^{-1} are attributed to the $E_{(1)}$ modes, which are responsible for the Raman spectra's $E_{(1)}$ bands. The $E_{(2)}$ mode, which is primarily distinguished by asymmetries along the c-axis, corresponds to the bands at 141 cm^{-1}. The broad bands are of the second order at 268.9 cm^{-1}[30–32]. Tellurium's characteristic peaks at 122 and 141 cm^{-1} can be seen in both 2.5% Te-LCO and 5% Te-LCO which corresponds to the A_1 bond-stretching mode and two degenerate

E bond-stretching modes, respectively [33]. There is a slight red shift for the high intensity Te peak in Te-LCO, and increasing the Te conc. broadens the peaks.

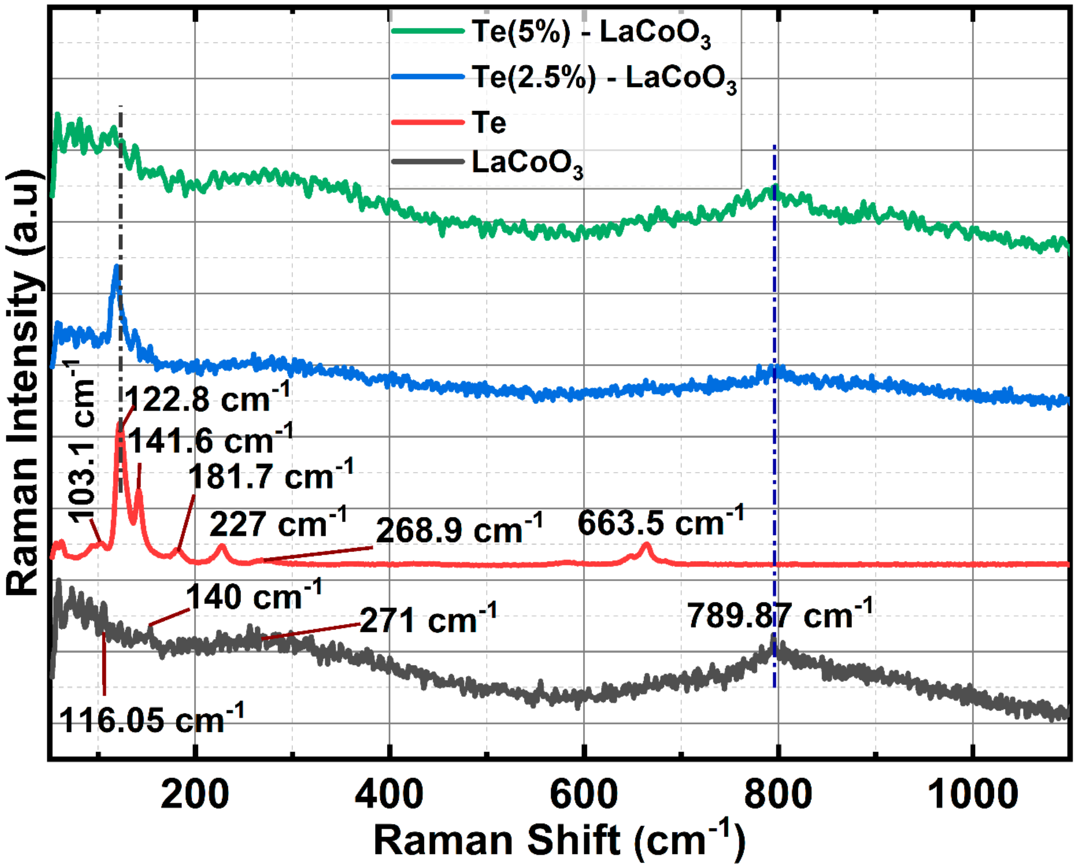

Figure 3. Raman spectroscopy of LCO, Te, 2.5% Te-LCO & 5% Te-LCO.

3.3. SEM and Energy-Dispersive X-Ray (EDS) Analysis of Te Incorporated LaCoO$_3$

Te-LCO composites are created by impregnating tellurium into the pores of LCO, which successfully preserves the material's irregular spherical shape. Figure 4 (a), (b), (c), (d), and (e) present the surface morphology of TeO$_2$, Te, LCO, 2.5% Te-LCO, and 5% Te-LCO, respectively. TeO$_2$ and Te show (Figure 4 a & b) that the reduction leads to the uniformly distributed plated nanostructure from mono-dispersed irregular microcrystals of about a few micrometres to nearly 500 nm. The hydrothermal synthesis of LCO (Figure 4 c) leads to a well dispersed spherical crystallite structure and the impregnating of Te in LCO (Figure 4 d & e) has impacted slightly on the microstructure. The Te impregnated LCO is well segregated, which is visible in the SEM micrograph. The EDAX spectrum of TeO$_2$, Te, LCO, 2.5% Te-LCO, and 5% Te-LCO is revealed in Figure 4, which confirms the occurrence of constituent elements.

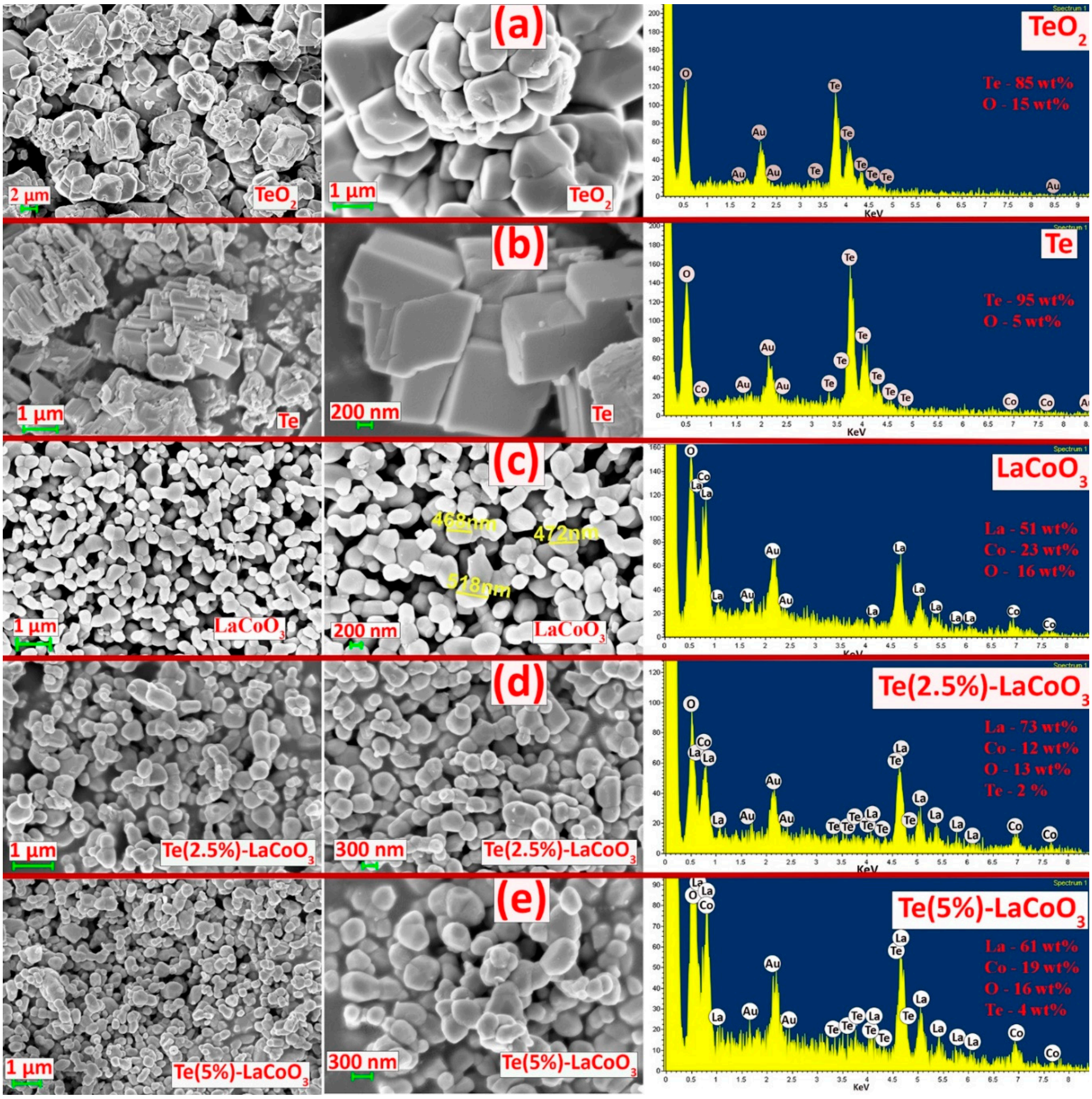

Figure 4. SEM and EDAX image of (a) TeO_2, (b) Te, (c) $LaCoO_3$, (d) Te(2.5%) - LCO and Te(5%) - LCO.

3.4. X-Ray Photoelectron Spectroscopy (XPS) studies of Te Incorporated $LaCoO_3$

X-ray photoelectron spectroscopy (XPS)is utilised to investigate the valence state of pure LCO and Te in-cooperated LCO with a Te content of 5 wt.%. The XPS survey spectra in Figure 5(a) and (d) demonstrate the presence of Co, O, La, and Te (5 wt.% Te in-cooperated LCO). Core-level XPS spectra verify the real valence states of the individual components. Co 2p core level spectra, both pure and Te in-cooperated, are shown in Figures 5 c and f, respectively. LCO's two asymmetric peaks are located at 780.18 and 795.45 eV and are most similar to those of Co $2p_{3/2}$ and Co $2p_{1/2}$. Paramagnetic Co^{2+} is formed at the surface, accounting for the visible satellite peaks above the primary photo peaks [34]. Because of the presence of numerous excitations and the coexistence of Co^{3+} and Co^{2+} states, the Co 2p peak expanded and shifted toward higher energy when Te was present in conjunction with LCO. The existence of both high-spin Co^{2+} and low-spin Co^{3+} ions were further validated by the appearance of the Co$2p_{3/2}$ peaks at 781.23 eV with decreased satellite peaks [35,36]. The Co 2p photoelectron spectra of Te-LCO are chemically shifted sufficiently to permit chemical identification. The Co $2p_{3/2}$ and Co $2p_{1/2}$ lines for Te-LCO were chemically shifted to 1.05 eV and 1.14 eV, respectively, to higher binding energies than for LCO. The Co $2p_{3/2}$ has diminished satellite peak may be due to well exposure of LCO when we mechanically ball mill with Te, which leads to further oxidation of

doi:10.20944/preprints202305.1993.v1

the samples towards the surface. According to research by Frost and colleagues [34,37], photoelectron spectra of high-spin Co^{2+} compounds show robust satellites, while those of low-spin Co^{2+} compounds either show weak satellites or none at all. Te-LCO has a core photoemission peak separation of 15.36 eV, while LCO's is 15.27 eV. These values are fairly close to the CoO and Co_3O_4 values that have previously been published [34,38] as depicted in Figure 5. As anticipated, the La 3d line shows the four component peaks (b and e). According to our prior research [19], the La $3d_{5/2}$ and La $3d_{3/2}$ are associated to the double peaks of LCO, which emerge at 834.7 and 838.34 eV, respectively. These peaks can be attributed to the La^{3+} state and represent charge transfer between the La_2O_3, O2p and La 4f orbits [36–38] or substantial electronic configuration final state mixing [42]. Te in-corporation causes a shift toward greater binding energies, indicating that the lattice structure is being destroyed. Because of Te's multivalence state, the additive peak with the highest intensity at 837.34 eV could be attributable to the synthesis of La sub-oxide (La-O_x). The observed core-level Te3d spectra have been deconvoluted into single $3d_{3/2}$ and $3d_{5/2}$ spin-state peaks at about 587 and 576 eV, respectively, to help explain it better.The chemical shift seen at Te $3d_{5/2}$ of approximately 3 eV towards higher binding energy from Te^{2-} is characteristics of $NaBH_4$ reduced TeO_2, which may form some surface oxidation layers (Te^0). Figure 5 (i) shows the two asymmetric peaks of high-resolution Te 3d XPS spectroscopy, which reveals the $Te^{4+}/Te^{2-}/Te^0$ oxidation state for the $NaBH_4$ reduced TeO_2.The binding energy difference between $3d_{3/2}$ and $3d_{5/2}$ is 10.4 eV, which agrees with the literature [43–45]. As was previously mentioned, the presence of Te at high oxidation states reconstructs the crystal structure and produces more Co^{2+} and Co^{3+} at various spin states, which leads to additional defects. The perovskite's A and B sites are both affected by the equally distributed Te^{4+}, which results in an increase in the amount of La^{2+} in the A site and an anisotropic Co^{2+} in the B site to balance the charge. As a result, the magnetic state of the perovskite LCO was affected by the discrete La 3d and Co 2p photoemission peaks that the 5% Te in-coordinated LCO displayed at various spin states [46,47]. The same O1s peaks associated with the LCO and 5% Te-LCO provide evidence that Te played a part in the incorrect perovskite oxide's formation. As demonstrated in Figure 5, both the pristine and Te-LCO O1s peaks had three unique peaks (h & g). O1s peaks observed at 528.8, 530.9, and 532.6 eV on the LCO surface. This major signal at 528.8 eV can be attributable to either bulk oxide or to lattice oxygen (O^{2-}), which is in line with the findings from earlier studies [41]. When looking at the oxide system, the broad peaks that have greater binding energies are the ones that are the most challenging to interpret. The value of 530.9 eV can be explained by the presence of chemisorbed oxygen (O^-) or adsorbed H_2O/OH^- species, both of which create a vacancy at the surface for oxygen to occupy [48].O 1s XPS spectra of the Te impregnated LCO surface show that superoxide (O^{2-}) formation occurs at a peak energy of 532.6 eV, while the other two peaks can be attributed to lattice oxygen, chemically adsorbed oxygen species on the oxygen vacancies, and physically adsorbed oxygen species on the surface. Three peaks with centres at BE = 529.5, 531.6, and 532.7 eV were revealed by deconvolution of the Te-impregnated LCO asymmetric O 1s spectra (Figure 5 g) [49]. These peaks correspond to lattice oxygen (such as O_2), chemically adsorbed oxygen (such as O^-), and physically adsorbed oxygen (H_2O, O_2), respectively. This encourages the conception of more peroxide/superoxide ions, which results in the acquisition of stronger peaks at 532.7 eV. Te^{4+} is in higher oxidation states in the Te in-cooperated LCO as a result of the exchange of oxygen species that occurs as oxygen vacancies form between bulk and surface oxides [40].

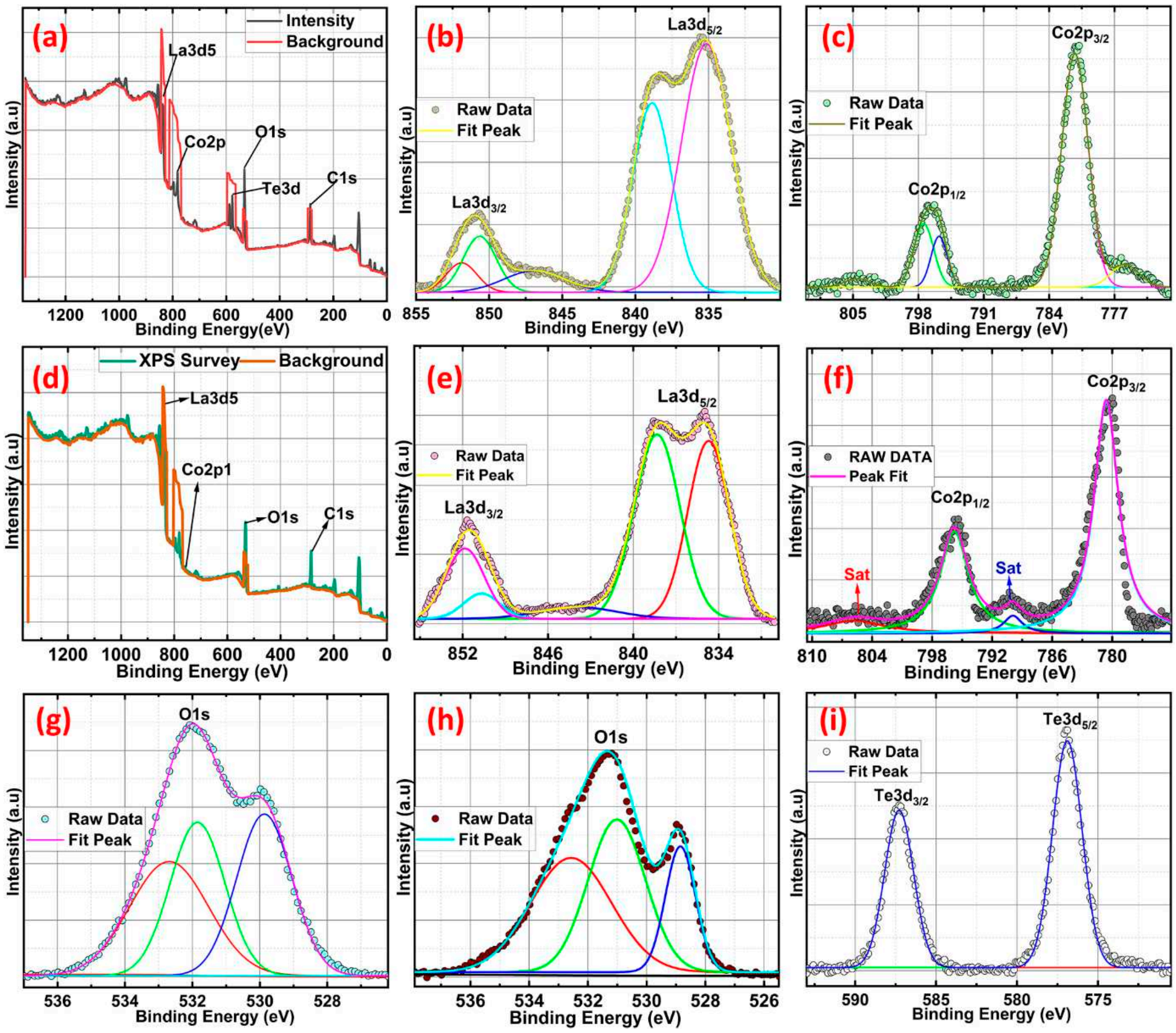

Figure 5. XPS Survey Scan (a & b) of LCO and Te(2.5%)-LCO respectively. Detail XPS scan of La 3d (b & e), Co 2p (c & f), O 1s (g & h) of LCO and Te(2.5%)-LCO respectively and Te 3d (i) of Te(2.5%)-LCO.

3.4. Magnetic Properties of Te Incorporated $LaCoO_3$

At 300 K, the field dependency of magnetization (M-H) for pristine LCO, 2.5% Te-LCO, and 5% Te-LCO was measured for a field change from -2.5 T to 2.5 T. The M-H loop at 300 K (Figure 6 a) suggests that the samples are originally in a paramagnetic state (LCO) and that the magnetic state changes to a weak ferromagnetic with the addition of Te, as shown in Figure 6 a, where the hysteresis develops with Te impregnation of LCO. When compared to the parent LCO, the overall magnetization value of the incubated samples is lower. The samples have a very low magnetic saturation (M_S) value after incorporation with Te. However, some previous studies relate the magnetic state to the anti-ferromagnetic exchange interaction in the samples [50], which arises from the antiferromagnetically ordered localized high spin states present in these systems with the incorporation of Te [51]. The values of magnetization (M_S), M_R and H_C extracted from the magnetic data (Figure 6) are given in Table 2. With the initial incorporation of 2.5% Te, it induces the coercivity and it decreases for higher concentrations of Te (5%). The anti-symmetric exchange interaction, which arises from the interaction of low spin Co (III) with the excited high spin Co (III). This further influences the magneto-crystallite anisotropy and reduces the coercive field [52]. In our previous study of Mn doped LCO, the RT M-H shows only a paramagnetic state even after incorporation with Mn at the Co site [19]. From the XPS study, it can be understood that the different valence states of Te may occupy La/Co sites, which enhances the magnetic property in the present LCO system.

Table 2. Saturation magnetization(M), remnant magnetization (M_R) and coercivity(H_C) of pure and Te@LCO.

Composition	H_C(T)	M (emu/g) @300K	M_R(emu/g)
LCO	--	---	-----
2.5% Te-LCO	0.0065	0.20166	0.00128
5% Te-LCO	0.0049	0.17051	0.00094

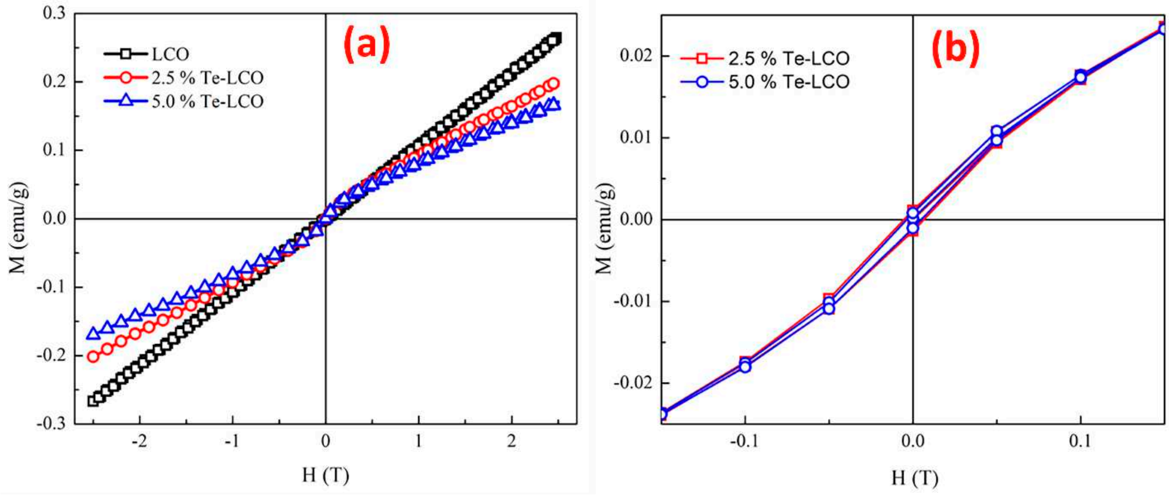

Figure 6. Isothermal magnetization curve of (a) LCO, 2.5% Te-LCO and 5% Te-LCO at RT and (b) enlarged image of LCO, 2.5% Te-LCO and 5% Te-LCO at RT. .

3.5. Transmission analysis of Te Incorporated $LaCoO_3$

Furthermore, TEM was used to verify the nanoparticle size and material structure. LCO Figure 7 (a and b), 2.5 wt.% Te-LCO (d and e), and 5 wt.% Te-LCO (g and h) demonstrate an evident ellipsoid structure with a 100-200 nm distribution in Figure 7. Due of the low Te concentration in LCO, lattice plane separation cannot be observed. In addition, Figure 7 shows the 5% Te-LCO's selected area electron diffraction (SAED) patterns. The composite reflected a single crystal structure with a few irregular brilliant spots, showing that the addition of Te affected the original structure of LCO [53]. Figure 7 depicts the interplanar spacing (d_{hkl}) measured from the SAED patterns.

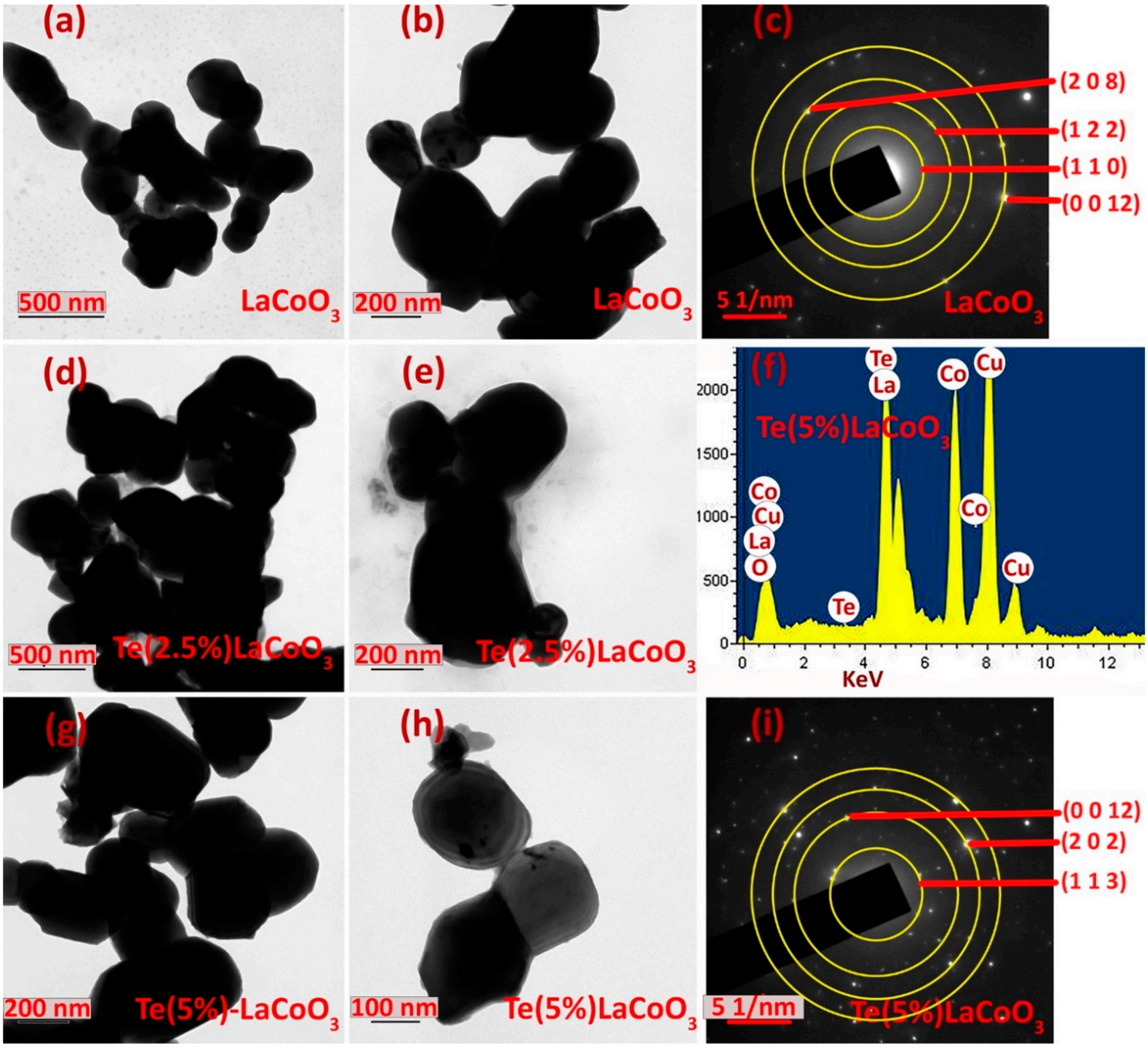

Figure 7. TEM image of (a & b) LaCoO3, (d & e) Te(2.5%) – LCO and (g & h) Te(5%) – LCO. SAED of (c) $LaCoO_3$, and (i) Te(5%) – LCO and EDS image of (f) Te(5%) – LCO.

4. Conclusion

The findings provide a systematic examination of Te impregnation in LCO perovskite oxide at various concentrations. As-prepared perovskite oxides have been analysed for their magnetic properties and crystal structures. The results showed that the samples exhibited an imperfect rhombohedral crystal structure. Adding Te to LCO produces a perovskite with a high multi-valence state of $Te^{4+/2-}$ and three distinct oxygen species where creates oxygen deficiency. Raman spectroscopy and XPS analysis both show that the presence of Te^{4+} prevents the formation of defective cobalt oxide. After being subjected to impact and iteration in a ball mill, the SEM micrograph of LCO and Te-impregnated LCO demonstrates structural similarity between the parent and included samples. However, XRD analysis revealed that Te-LCO was successfully reduced and incorporated into the mixture as a result of the ball mill's influence on the crystallite structure. The structural integrity of the perovskite samples has also been verified using transmission electron microscopy investigation. The presence of weak ferromagnetic order at ambient temperature after impregnation implies its potential application in magnetic devices and hypersonic vehicles.

Data Availability All the data used in the manuscript are within the manuscript.

Conflicts of Interest The authors declare that they have no conflicts of interest.

Acknowledgments The authors would like to thank the National Research Foundation of Korea (NRF) grant, funded by the Korean government (MIST) (No. 2022R1C1C1006414) and (No.2021R1A4A1032207). The author SEM acknowledges the funding agency of SERB-TARE fellowship (TAR/2021/000097).

References

1. N Fist, J Dinan, R Stadelmannand N Orlovskaya, (2012) "In situ three point bending device for measurements of vibrational response of ceramics under stress by microRaman spectroscopy," Advances in Applied Ceramics, vol. 111, no. 7, pp. 433-439, 2012.https://doi.org/10.1179/1743676111Y.0000000069
2. C.B Samantaray, H Sim, and H Hwang, "Electronic structure and optical properties of barium strontium titanate ($Ba_xSr_{1-x}TiO_3$) using first-principles method,"Physica B: Condensed Matter, vol. 351, no. 1-2, pp. 158-162, 2004. https://doi.org/10.1016/j.physb.2004.05.025
3. C.B. Samantaray, H. Sim, and H. Hwang, "The electronic structures and optical properties of $BaTiO_3$ and $SrTiO_3$ using first-principles calculations," Microelectronics Journal, vol. 36, no. 8, pp.725-728, 2005. https://doi.org/10.1016/j.mejo.2005.03.001
4. J. G. Bednorz, and K. A. Müller, "$Sr_{1-x}Ca_xTiO_3$: An XY Quantum Ferroelectric with Transition to Randomness," Physical Review Letters, vol. 52, pp. 2289-2292, 1984. https://doi.org/10.1103/PhysRevLett.52.2289
5. H. P. R. Frederikse, W. R. Thurber, and W. R. Hosler, "Electronic Transport in Strontium Titanate," Physical Review Journals Archive, vol. 134, pp. A442-A445, 1964. https://doi.org/10.1103/PhysRev.134.A442
6. C. S. Koonce, M. L. Cohen, J. F. Schooley, W. R. Hosler, and E. R. Pfeiffer, "Superconducting Transition Temperatures of Semiconducting SrTiO3,"Physical Review Journals Archive, vol. 163, pp. 380-390, 1967. https://doi.org/10.1103/PhysRev.163.380
7. H. Wang, B. Wang, Q. Li, Z. Zhu, R. Wang, and C. H. Woo, "First-principles study of the cubic perovskites $BiMO_3$ (M=Al, Ga, In, and Sc)," Physical Review B,vol. 75, pp. 245209, 2007. https://doi.org/10.1103/PhysRevB.75.245209
8. P. Baettig, C.F. Schelle, R. LeSar, U. V. Waghmare, and N.A. Spaldin, "Theoretical prediction of new high-performance lead-free Piezoelectrics," Chemistry of Materials, vol. 17, pp. 1376–1380, 2005. https://doi.org/10.1021/cm0480418
9. H. Muta, K. Kurosaki, and S. Yamanaka, "Thermoelectric properties of rare earth doped $SrTiO_3$," Journal of Alloys and Compounds, vol. 350, no. 1-2, pp. 292-295, 2003. https://doi.org/10.1016/S0925-8388(02)00972-6
10. P. Sivaprakash, S.Divya, R.Parameshwari,C. Saravanan, S.Sagadevan, S. Arumugam and S. Esakki Muthu,"Influence of Zn^{2+} doping towards the structural, magnetic, and dielectric properties of $NiFe_2O_4$ composite. Journal of Materials Science: Materials in Electronics,vol. 31, pp. 16369–16378, 2020. https://doi.org/10.1007/s10854-020-04187-9
11. A. J. Millis, Boris I. Shraiman, and R. Mueller, "Dynamic Jahn-Teller Effect and Colossal Magnetoresistance in $La_{1-x}Sr_xMnO_3$," Physical Review Letters, vol. 77, 175-178, 1996.https://doi.org/10.1103/PhysRevLett.77.175
12. S. Divya, P. Sivaprakash, S. Raja, S. Esakki Muthu, Emad M. Eed, S. Arumugam and Tae Hwan Oh, "Temperature-dependent dielectric and magnetic properties of $NiFe_2O_4$ nanoparticles," Applied Nanoscience, 2021. https://doi.org/10.1007/s13204-021-02026-9
13. M. Dragan, S. Enache, M. Varlam, and K. Petrov, "Perovskite-Type Lanthanum Cobaltite $LaCoO_3$: Aspects of Processing Route toward Practical Applications," Cobalt Compounds and Applications, IntechOpen, 2019. http://dx.doi.org/10.5772/intechopen.86260
14. H. Hilgenkamp, Ariando, H.J.H. Smilde, D.H.A. Blank, G. Rijnders, H. Rogalla, J.R. Kirtley, and C.C. Tsuel, "Ordering and manipulation of the magnetic moments in large-scale superconducting π-loop arrays," Nature, vol. 422, pp. 50–53, 2003. https://doi.org/10.1038/nature01442
15. P. M. Raccah, and J. B. Goodenough, "First-Order Localized-Electron ⇆ Collective-Electron Transition in $LaCoO_3$," Physical Review Journals Archive,vol. 155, pp. 932-943, 1967. https://doi.org/10.1103/PhysRev.155.932
16. M.A. Señarís-Rodríguez, and J.B. Goodenough, "Magnetic and Transport Properties of the System $La_{1-x}Sr_xCoO_{3-\delta}$ $(0 < x \le 0.50)$," Journal of Solid State Chemistry,vol. 118, pp. 323–336, 1995. https://doi.org/10.1006/JSSC.1995.1351

17. A. Maignan, D. Flahaut, and S. Hebert, "Sign change of the thermoelectric power in $LaCoO_3$," The European Physical Journal B - Condensed Matter and Complex Systems, vol. 39, pp. 145–148, 2004. https://doi.org/10.1140/epjb/e2004-00179-8
18. E. J. Guo, R. Desautels, D.Keavney, M. A. Roldan, B. J. Kirby, D. Lee, Z. Liao, T. Charlton, A.Herklotz, T. Z. Ward, M. R. Fitzsimmons, andH. N. Lee, "Nanoscale ferroelastic twins formed in strained $LaCoO_3$ films," Science advances, vol. 5, pp. 1-5, 2019. https://doi.org/10.1126/sciadv.aav5050
19. S. Jhelai, M. Radhakrishnan, N. Padmanathan, S. Esakki Muthu, P. Sivaprakash, and M. Kadiresan, "Effect of Mn substitution on magnetic behaviour of oxygen defective $LaCoO_3$ perovskite oxide," Materials Science and Engineering: B, vol. 284, pp. 115875, 2022. https://doi.org/10.1016/j.mseb.2022.115875
20. J.S. Zhou, J.Q. Yan, and J.B. Goodenough, "Bulk modulus anomaly in $RCoO_3$ (R=La, Pr, and Nd)," Physical Review B - Condensed Matter and Materials Physics, vol. 71, pp. 22010, 2005. https://doi.org/10.1103/PhysRevB.71.220103
21. T. Vogt, J.A. Hriljac, N.C. Hyatt, and P. Woodward, "Pressure-induced intermediate-to-low spin state transition in $LaCoO_3$," Physical Review B- Condensed Matter and Materials Physics, vol. 67, pp. 140401, 2003. https://doi.org/10.1103/PhysRevB.67.140401
22. S. Divya, P. Sivaprakash, S. Raja, S. Esakki Muthu, Ikhyun Kim, N. Renuka, S. Arumugam, and Tae Hwan Oh, "Impact of Zn doping on the dielectric and magnetic properties of $CoFe_2O_4$ nanoparticles," Ceramics International, vol. 48,pp. 33208-33218, 2022. https://doi.org/10.1016/j.ceramint.2022.07.263
23. Y. Xu, P. Zielke, N. van Nong, S. Pirou, R. Reolon, X. Si, S.B. Simonsen, P. Norby, H. Lühmann, W. Bensch, and R. Kiebach, "Hydrothermal Synthesis, Characterization, and Sintering Behavior of Core-Shell Particles: A PrincipleStudy on Lanthanum Strontium Cobaltite Coated with Nanosized Gadolinium Doped Ceria," Ceramics. vol.1,pp. 246-260, 2018. https://doi.org/10.3390/ceramics1020020
24. M. Ayyob, I. Ahmad, F. Hussain, M. Kashif Bangash, J.A. Awan, and J.N. Jaubert, "A new technique for the synthesis of lanthanum substituted nickel cobaltite nanocomposites for the photo catalytic degradation of organic dyes in wastewater," Arabian Journal of Chemistry,vol. 13, pp. 6341–6347, 2020. https://doi.org/10.1016/j.arabjc.2020.05.036
25. Deeksha, P. Kour, I. Ahmed, K. K.Haldar,and K. Yadav, "Tuning the Morphology of Lanthanum Cobaltite Using the Surfactant-Assisted Hydrothermal Approach for Enhancing Oxygen Evolution Catalysis," Proceedings of the National Workshop on Recent Advances in Condensed Matter and High Energy Physics, Springer Proceedings in Physics, Springer, Singapore,vol. 278, pp. 15-24, 2022. https://doi.org/10.1007/978-981-19-2592-4_2
26. L. Tepech-Carrillo, A. Escobedo-Morales, A. Pérez-Centeno, E. Chigo-Anota, J.F. Sánchez-Ramírez, E. López-Apreza, and J. Gutiérrez-Gutiérrez, "Preparation of Nanosized $LaCoO_3$ through Calcination of a Hydrothermally Synthesized Precursor," Journal of Nanomaterials,vol. 2016, pp. 7, 2016. https://doi.org/10.1155/2016/6917950
27. M. Popa, J. Frantti, and M. Kakihana, "Characterization of $LaMeO_3$ (Me: Mn, Co, Fe) perovskite powders obtained by polymerizable complex method," Solid State Ionics. Vol. 154–155, pp. 135-141, 2002. https://doi.org/10.1016/S0167-2738(02)00421-6
28. M.N. Iliev, and M. V Abrashev, "Raman phonons and Raman Jahn-Teller bands in perovskite-like manganites," Journal of Raman Spectroscopy, vol. 32, no. 10, pp. 805–811, 2001. https://doi.org/10.1002/jrs.770
29. N. Orlovskaya, D. Steinmetz, S. Yarmolenko, D. Pai, J. Sankar, and J. Goodenough, "Detection of temperature- and stress-induced modifications of $LaCoO_3$ by micro-Raman spectroscopy,"Physical Review B - Condensed Matter and Materials Physics, vol. 72, pp. 014122, 2005. https://doi.org/10.1103/PhysRevB.72.014122
30. R.M. Martin, G.I. Ucovsky, and K. Helliwell, "Intermolecnlar bonding and lattice dynamics of Se and Te," Physical Review B - Condensed Matter and Materials Physics, vol. 13, pp. 1383, 1976. https://doi.org/10.1103/PhysRevB.13.1383
31. A. S. Pine and G. Dresselhaus, "Raman Scattering in Paratellurite, TeO_2," Physical Review B - Condensed Matter and Materials Physics, vol. 5, pp. 4087, 1972. https://doi.org/10.1103/PhysRevB.5.4087
32. C. Marini, D. Chermisi, M. Lavagnini, D. Di Castro, C. Petrillo, L. Degiorgi, S. Scandolo, and P. Postorino, "High-pressure phases of crystallite tellurium: A combined Raman and ab initio study,"Physical Review B - Condensed Matter and Materials Physics, vol. 86. Pp. 064103, 2012. https://doi.org/10.1103/PhysRevB.86.064103

33. J. He, W. Lv, Y. Chen, K. Wen, C. Xu, W. Zhang, Y. Li, W. Qin, and W. He, "Tellurium-Impregnated Porous Cobalt-Doped Carbon Polyhedra as Superior Cathodes for Lithium-Tellurium Batteries," ACS Nano,vol. 11, pp. 8144–8152, 2017. https://doi.org/10.1021/acsnano.7b03057
34. J. Haber, and L. Ungier, "On chemical shifts of ESCA and Auger lines in cobalt oxides,"Journal of Electron Spectroscopy and Related Phenomena, vol. 12,pp. 305-312, 1977.https://doi.org/10.1016/0368-2048(77)85081-0
35. N. S. McIntyre, D. D. Johnston, L. L.Coatsworth, R. D. Davidson, and J. R. Brown, "X-ray photoelectron spectroscopic studies of thin film oxides of cobalt and molybdenum," Surface and Interface Analysis, vol. 15, no. 4, pp. 265-272, 1990. https://doi.org/10.1002/sia.740150406
36. H. Wang, W. Xu, S. Richins, K. Liaw, L. Yan, M. Zhou, and H. Luo, "Polymer-assisted approach to $LaCo_{1-x}Ni_xO_3$ network nanostructures as bifunctional oxygen electrocatalysts," Electrochimica Acta, vol. 296, pp. 945–953, 2019. https://doi.org/10.1016/j.electacta.2018.11.075
37. D.C. Frost, C.A. McDowell, and I.S. Woolsey, "Evidence for multiplet splitting of 2p photoelectron lines of transition metal complexes," Chemical Physics Letters, vol. 17, pp. 320-323, 1972. https://doi.org/10.1016/0009-2614(72)87086-6
38. H. Seim, M. Nieminen, L. Niinistö, H. Fjellvåg, and L.S. Johansson, "Growth of $LaCoO_3$ thin films from β-diketonate precursors," Applied Surface Science, pp. 112, pp. 243–250, 1997. https://doi.org/10.1016/S0169-4332(96)01001-X
39. C. V. Ramana, R.S. Vemuri, V. V. Kaichev, V.A. Kochubey, A.A. Saraev, and V. V. Atuchin, "X-ray photoelectron spectroscopy depth profiling of La_2O_3/Si thin films deposited by reactive magnetron sputtering," ACS Applied Materialsand Interfaces, vol. 3, pp. 4370–4373, 2011. https://doi.org/10.1021/am201021m
40. X. Jiang, Y. Dong, Z. Zhang, J. Li, J. Qian, and D. Gao, "Cation substitution of B-site in $LaCoO_3$ for bifunctional oxygen electrocatalytic activities," Journalof Alloys and Compounds,vol. 878, pp. 160433, 2021. https://doi.org/10.1016/J.JALLCOM.2021.160433
41. L. Armelao, D. Barreca, G. Bottaro, A. Gasparotto, C. Maragno, and E. Tondello, "$LaCoO_3$Nanosystems by a Hybrid CVD/Sol-Gel Route: An XPS Investigation," Surface Science Spectra,vol. 10, pp. 143–149, 2003. https://doi.org/10.1116/11.20040303
42. R. P. Vasquez, "X-ray photoemission measurements of $La_{1-x}Ca_xCoO_3$(x=0, 0.5)," Physical Review B - Condensed Matter and Materials Physics, vol. 54, pp. 14938, 1996. https://doi.org/10.1103/PhysRevB.54.14938
43. A.J. Ricco, H.S. White, and M.S. Wrighton, "X-ray photoelectron and Auger electron spectroscopic study of the CdTe surface resulting from various surface pretreatments: Correlation of photoelectrochemical and capacitance-potential behavior with surface chemical composition," Journal of Vacuum Science & Technology A: Vacuum, Surfaces, and Films, vol. 2, pp. 910–915, 1984. https://doi.org/10.1116/1.572547
44. A.B. Christie, I. Sutherland, and J.M. Walls, "Studies of the composition, ion-induced reduction and preferential sputtering of anodic oxide films on $Hg_{0.8}Cd_{0.2}Te$ by XPS," Surface Science, vol. 135, no. 1-3, pp. 225-242, 1983. https://doi.org/10.1016/0039-6028(83)90220-0
45. K. Hidetaka, and Y. Yoshihisa, "Ylide-Metal Complexes. XIV. An X-Ray Photoelectron Spectroscopic Study on Tellurium Complexes of Methylenetriphenylphosphorane," Bulletin of the Chemical Society of Japan,vol. 61, no. 8, pp. 2990-2992, 1988. https://doi.org/10.1246/bcsj.61.2990
46. W. Branford, M.A. Green, and D.A. Neumann, "Structure and ferromagnetism in Mn^{4+}spinels: $AM_{0.5}Mn_{1.5}O_4$ (A = Li, Cu; M = Ni, Mg)," Chemistry of Materials, vol. 14, no. 4, pp. 1649–1656, 2002. https://doi.org/10.1021/cm010857a
47. K.P. Thummer, M.C. Chhantbar, K. Modi, and H. Joshi, Effect of Mn^{4+} substitution on magnetic behaviour of cobalt ferrite, Indian Journal of Physics, vol. 79, pp. 41–45, 2005.
48. H. Liang, Y. Hong, C. Zhu, S. Li, Y. Chen, Z. Liu, and D. Ye, "Influence of partial Mn-substitution on surface oxygen species of $LaCoO_3$ catalysts," Catalysis Today,vol. 201, pp. 98–102, 2013. https://doi.org/10.1016/J.CATTOD.2012.04.036
49. P. Xiao, J. Zhu, H. Li, W. Jiang, T. Wang, Y. Zhu, Y. Zhao, and J. Li, "Effect of textural structure on the catalytic performance of $LaCoO_3$ for CO oxidation,"ChemCatChem, vol. 6, no. 6,pp. 1774–1781, 2014. https://doi.org/10.1002/cctc.201402064

doi:10.20944/preprints202305.1993.v1

50. R. Schmidt, J. Wu, C. Leighton, and I. Terry, Dielectric response to the low-temperature magnetic defect structure and spin state transition in polycrystalline $LaCoO_3$," Physical Review B - Condensed Matter and Materials Physics,vol. 79, pp. 125105, 2009. https://doi.org/10.1103/PhysRevB.79.125105
51. K. Tomiyasu, M. Sato, S.I. Koyama, T. Nojima, R. Kajimoto, S. Ji, and K. Iwasa, "Magnetic properties of electron-doped $LaCoO_3$," Journal of the Physical Society of Japan, vol. 86, no. 9, pp. 094706, 2017. https://doi.org/10.7566/JPSJ.86.094706
52. D. Gignoux, Etienne Du Tremolet De Lacheisserie, M. Schlenker, "Magnetism: Materials and Applications," Springer. 0-387-23063-7 (2005).
53. R. Wang, C. Ye, H. Wang, and F. Jiang, "Z-Scheme $LaCoO_3$/g-C_3N_4 for Efficient Full-Spectrum Light-Simulated Solar Photocatalytic Hydrogen Generation," ACS Omega. vol. 5, no. 47, pp. 30373–30382, 2020. https://doi.org/10.1021/acsomega.0c03318